Cell-Directed Integration into Three-Dimensional Lipid–Silica Nanostructured Matrices

Jason C. Harper,[†,§] Constantine Y. Khirpin,[†] Eric C. Carnes,[†] Carlee E. Ashley,[†] DeAnna M. Lopez,[§] Travis Savage,[†] Howland D. T. Jones,[§] Ryan W. Davis,[§] Dominique E. Nunez,[†] Lina M. Brinker,[†] Bryan Kaehr,[§] Susan M. Brozik,[†,§,*] and C. Jeffrey Brinker[†,‡,§,*]

[†]Departments of Chemical and Nuclear Engineering and [‡]Molecular Genetics and Microbiology, University of New Mexico, Albuquerque, New Mexico 87131 and [§]Sandia National Laboratories, Albuquerque, New Mexico 87106

ABSTRACT We report a unique approach in which living cells direct their integration into 3D solid-state nanostructures. Yeast cells deposited on a weakly condensed lipid/silica thin film mesophase actively reconstruct the surface to create a fully 3D bio/nano interface, composed of localized lipid bilayers enveloped by a lipid/silica mesophase, through a self-catalyzed silica condensation process. Remarkably, this integration process selects exclusively for living cells over the corresponding apoptotic cells (those undergoing programmed cell death), *via* the development of a pH gradient, which catalyzes silica deposition and the formation of a coherent interface between the cell and surrounding silica matrix. Added long-chain lipids or auxiliary nanocomponents are localized within the pH gradient, allowing the development of complex active and accessible bio/nano interfaces not achievable by other synthetic methods. Overall, this approach provides the first demonstration of active cell-directed integration into a nominally solid-state three-dimensional architecture. It promises a new means to integrate "bio" with "nano" into platforms useful to study and manipulate cellular behavior at the individual cell level and to interface living organisms with electronics, photonics, and fluidics.

KEYWORDS: sol–gel · mesoporous silica · biomaterials · cell encapsulation/entrapment · cell-directed integration · evaporation-induced self-assembly

The generation of new 3D matrices that enable integration of biomolecular components and whole cells into device architectures, without adversely altering their morphology or activity, continues to be an expanding and challenging field of research.[1–5] This research is driven by the promise that encapsulated biomolecules and cells can significantly impact areas as diverse as biocatalysis, controlled delivery of therapeutics, environmental and industrial process monitoring, early warning of warfare agents, bioelectronics, and tissue/organ replacement.[6–9] To date, extensive techniques have been developed for biomolecule encapsulation generally relying on adsorption, covalent binding, or entrapment of biomolecules in polymeric materials.[10] Successful strategies for protein and enzyme entrapment are widely reported; however, encapsulation of living cells is significantly more challenging.[11,12] This is due to the more stringent requirements for the encapsulation matrix which must provide a functional bio/nano interface between the cells and the macroenvironment, protecting the cells from mechanical and chemical stresses, providing access to oxygen, nutrients, and target molecules of interest, and allowing for the expulsion of metabolic wastes.[13]

Silica matrices formed by sol–gel processing have been employed for cellular encapsulation beginning with the pioneering work of Carturan, who encapsulated *Saccharomyces cerivisiae* in a tetraethylorthosilicate (TEOS)-derived silica gel.[14] Advantages of physical entrapment of biomolecules and cells within wet (water or buffer-filled) silica gels include the ability of sol–gel systems to retain water with negligible swelling, biological inertness, mechanical stability, simple room temperature processing, and 3D confinement within a matrix that maintains accessibility of the cell.[7,15] Traditional sol–gel processing techniques, however, can be cytotoxic to cells. Exposure to alcohol solvents and byproducts, contact with polar chemical groups at the silica surface (*i.e.*, silanols), compressive stresses resulting from gel syneresis at neutral pH, and drying-induced tensile capillary stresses can damage the cell/gel interface and induce cell lysis. Therefore, strategies have been developed to mitigate these issues, including reducing the contact time between cells and the sol–gel precursor solution,[16,17] incorporating ameliorants (*i.e.*, gelatin, polyvinyl alcohol, glycersol) into the silica gel,[18–20] developing silicates with noncytotoxic hydrolysis and condensation byproducts (*i.e.*, poly(glyceryl)silicate),[21] using all aqueous precursors

*Address correspondence to smbrozi@sandia.gov, cjbrink@sandia.gov.

Received for review July 22, 2010 and accepted September 10, 2010.

10.1021/nn101793u

such as sodium silicate or colloidal silica,[22−24] or depositing thin silica films over cells *via* exposure to gas-phase silicon alkoxides.[8,25,26]

All of the sol−gel encapsulation strategies listed above result in the physical entrapment of cells with no evidence of cellular influence on the development of the matrix or bio/nano interface. As an alternative approach, we recently reported the cell-directed encapsulation of yeast and bacterial cells within a self-assembled biocompatible silica matrix.[27,28] Incorporation of short-chained phospholipids, in lieu of traditionally used surfactants which are cytotoxic to cells, during evaporation-induced self-assembly (EISA),[29] yielded an ordered silica mesophase within which incorporated cells actively organized a unique bio/nano interface and globally altered the matrix nanostructure. The bio/nano interface is composed of a multilayered lipid membrane that interfaces coherently with a 3D lipid-templated silica matrix, which provides accessibility of the encapsulated cells to molecules introduced into the 3D silica host.[28,30] Importantly, a localized nanostructured microenvironment was created in which 3D chemical gradients were established. Such gradients can provide an instructive background needed to achieve proper functionality and guide cellular behavior.[31,32] Examples include cell differentiation, biofilm formation, and quorum sensing, which all rely on the development of spatiotemporal gradients of signaling molecules.[30,33,34]

Herein we describe an extension of this original cell-directed assembly approach in which introduction of cells onto a preformed lipid-templated silica film leads to partial dissolution of matrix components and active cellular reconstruction of a 3D bio/nano interface composed of lipid-rich silica shells that interface the cells with the nanostructured inorganic matrix. Advantages to this new approach include (i) reduced stresses exerted on the cells due to avoidance of cellular contact with alcoholic solvents, byproducts, and catalysts; (ii) maintenance of the original nanostructure of the bulk film, providing greater control over the properties of host matrix; (iii) accessibility to the external environment *via* rapid transport through the thin film encapsulating the cells; (iv) improved optical accessibility through the thin film to interrogate the integrated cells; and (v) greater control over location of cells in the thin film. To our knowledge, this is the first example of active cell-directed integration into a nominally solid-state three-dimensional architecture. This report focuses on the general properties of the encapsulation matrix and the fundamental nanomaterial and biochemical mechanisms that govern this self-integration process.

RESULTS AND DISCUSSION

The living-cell-directed integration process is depicted in Scheme 1. Upon introduction of an aqueous suspension of *S. cerevisiae* cells (*via* pipet or aerosol) onto a weakly condensed lipid−silica mesophase film, components of the film are solubilized by the droplet (Scheme 1a). Upon evaporation, gradients in temperature, concentration, and viscosity lead to circulating Marangoni flows driven by surface tension gradients. Fluorescent microscopy video imaging of initial droplet evaporation using fluorescently stained cells shows that flow near the liquid−solid interface was driven toward the circumferential three-phase boundary, while flow near the liquid−gas interface was directed radially toward the droplet center in a circulating fashion (Scheme 1a).[35−38] The three-phase boundary was observed to de-pin immediately upon droplet deposition due to concentration of solubilized lipid, which presumably formed a Gibb's monolayer, while reducing the droplet surface tension (and contact angle) to below the receding angle value.

As evaporation proceeded, the three-phase boundary continued to recede with decreased contact area and nearly constant contact angle, while cells, lipid, and soluble silica were progressively concentrated within the droplet (Scheme 1b). Upon final droplet evaporation, as the film thickness became commensurate with the cell diameter, the slowly receding three-phase boundary was violently retracted by the meniscus curvature. This left clusters or single cells at the center of multiple droplets, containing high concentrations of lipid and soluble silica. Additionally, "coffee-stain rings"[36,38] of cells, lipid, and silica were often produced at the retracted droplet periphery, far within the original droplet edge. At this stage, viable cells develop a localized three-dimensional (3D) gradient in pH, catalyzing silica condensation, and their self-integration into a 3D lipid−silica nanostructure (Scheme 1c). Rinsing the substrate shortly after droplet evaporation removes uncondensed silica and lipid concentrate, leaving cells encapsulated in a coherent and conformal lipid-rich silica shell bound to the underlying film (Scheme 1d, and inset AFM image). In the following, we provide further detail and discussion of the successive stages of the cell integration process.

Lipid−Silica Matrix Solubilization and Reconstruction. Dissolution of lipid from the film following droplet introduction (Scheme 1a) was monitored by incorporation of 0.1% fluorescently labeled NBD-*di*C_6 PC lipid molecules (green emission) into the film and observing the fluorescence intensity upon exposure to water. The fluorescence microscopy image shown in Figure 1A contains three regions of interest: (i) pristine film, (ii) an area exposed to a water droplet for 10 min (water droplet is present in Figure 1A), and (iii) a scratched area where the film was entirely removed. Brief exposure of the weakly condensed lipid−silica film to the water droplet resulted in nearly complete loss of fluorescence intensity, as shown in region (ii). This loss of fluorescence is attributed to rapid lipid dissolution and, to a lesser ex-

tent, silica dissolution, which occurs more slowly and depends on film aging time (see following discussion). If left to evaporate, substantial fluorescence emission was recovered; however, in this case, the observed fluorescence in the water exposed and evaporated region was no longer homogeneous. Restoration of fluorescence in this nonhomogenous manner is characteristic of lipid and silica deposits following diffusion fronts during droplet evaporation. The solubility of the film components was further characterized by AFM imaging (Figure 1B), which shows that film areas exposed to water are reduced in thickness during contact with water and subsequent drying of the drop. The film thickness decrease is attributed to silica dissolution along with possible capillary stress-induced shrinkage or collapse of the mesoporous film during drying. *In situ* AFM imaging (Figure 3C) shows that, for films aged 30 min prior to introduction of water, the film thickness decreases upon water exposure and further upon drying. The latter shrinkage is attributed to capillary stresses imposed during drying of the porous lipid-depleted film.

Silica dissolution depends strongly on the aging time of the film and, thereby, its extent of condensation prior to introduction of the water drop. This is shown in Figure 1D, which plots the fraction of the film solubilized (determined by the molybdic blue assay of soluble silica; see Experimental Section) as a function of film aging time. Between 10 and 45% of the total film silica can be solubilized if water is introduced to the film during the first 10 min following film formation. Dissolution of this substantial portion of silica had a detrimental affect on the film morphology and uniformity. The fraction of silica solubilized from the film continued to decrease with film age, stabilizing near 1% at 30 min following film formation. These observations indicate that silica precursors in the prepared films continue to condense over time, reducing solubility.[39,40] Films aged for at least 30 min were structurally stable, maintaining uniformity and nanostructure following introduction of water droplets. On the basis of these results, lipid-templated mesoporous silica films were aged between 30 and 120 min prior to the introducion of an aqueous suspensions of cells.

Grazing-incidence small-angle X-ray scattering (GISAXS) and scanning electron microscopy (SEM) were used to characterize the lipid-templated silica matrix. The GISAXS pattern in Figure 2A, obtained for the as-deposited film, is consistent with a hexagonally ordered lipid−silica mesophase composed of lipid-filled cylindrical pores ~2.3 nm in diameter, with repeat distances (d_y) of ~3.0 nm perpendicular to the substrate and d_x of ~3.5 nm in the plane of the substrate. Figure 2B shows the GISAXS pattern recorded from a film in which yeast cells were introduced across the entire substrate *via* aerosol deposition. In contrast to our previous report in which cells and lipids were mixed directly with silica sols, resulting in a cell-directed hexagonal to

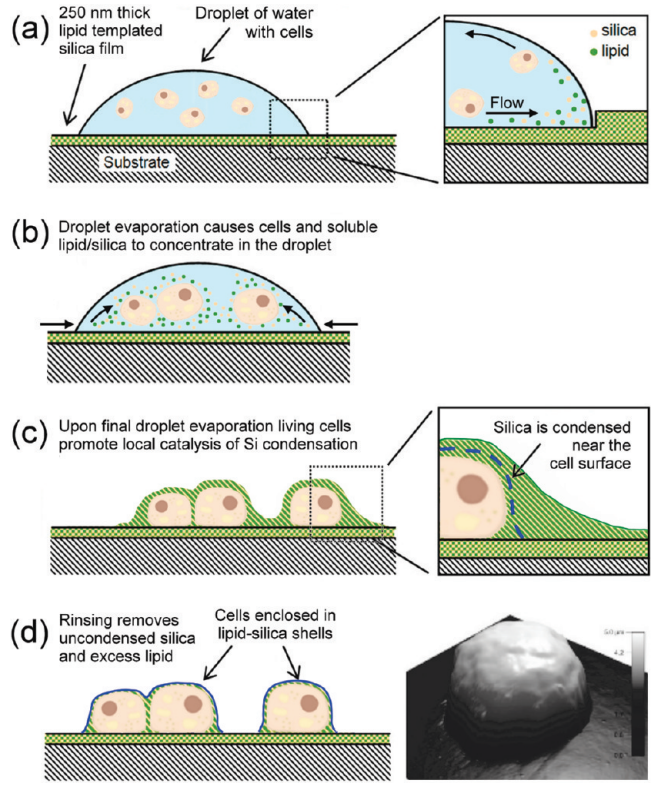

Scheme 1. Cell-directed integration of microorganisms in preformed lipid-templated silica thin films occurs *via* (a) initial solubilization of the slowly condensing film components (lipid and silica) upon introduction of an aqueous suspension of cells. Droplet evaporation leads to capillary and Marangoni flow, which concentrates cells and soluble components (b). Viable cells create a locally high pH, catalyzing silica condensation and their self-integration into a 3D lipid−silica nanostructure (c). Rinsing the substrate following droplet evaporation removes excess lipid and noncondensed silica, yielding cells encapsulated in a lipid-rich silica shell (d). The inset image was generated *via* atomic force microscopy of a single *S. cerevisiae* cell encapsulated in a lipid−silica shell following substrate rinsing. Scale bar = 0−5 μm.

lamellar phase transformation upon spin-coating,[27] the bulk hexagonal nanostructure of the preformed silica film was largely retained following introduction of the cells. This is not surprising as film dissolution and reorganization occurs only in the areas (~1% of total film area) exposed to the aerosol of the aqueous cell suspension. A slight loss of order of the primary hexagonal structure in the GISAXS pattern was accompanied by the development of a minor lamellar structure, similar to that observed in our previous work.[27] This suggests that the matrix is reorganized to form a lamellar structure local to the encapsulated cells, while the nanostructure of the bulk film remains unchanged. We have previously shown that self-assembly of amphiphilic template molecules occurs in the aqueous phase.[41] In that work, we showed for systems initially formed from a binary solvent (water and alcohol) that the alcohol cosolvent evaporates in the first stage of EISA, leaving self-assembly in the final stages of EISA to occur under completely aqueous conditions. In the case of a purely aqueous droplet extracting lipid and silica from the film, we also expect EISA to yield an or-

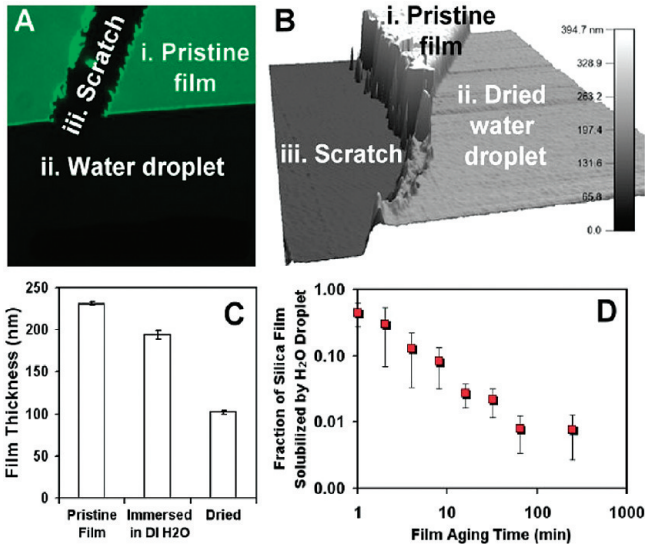

Figure 1. (A) Fluorescence microscopy image of a lipid-templated (0.1% NBD-labeled *di*C_6 PC, green emission) mesoporous silica film (i), upon introduction of a 0.5 μL water droplet (ii), near a scratch (iii) to expose the underlying substrate. (B) AFM measurement of the region imaged in (A). Scale bar = 0−395 nm. (C) AFM measured thickness of lipid-templated mesoporous silica films under various conditions. (D) Fraction of silica film solubilized *vs* age of the slowly condensing film as determined by molybdic acid assay.

dered nanostructure. The formation of a lamellar phase is consistent with the higher concentration of lipid in the aqueous droplet *versus* the lipid concentration in the initial sol precursor solution.

SEM imaging was performed directly (without fixation or supercritical drying) on silicon substrates coated with lipid-templated silica films onto which *S. cerevisiae* cells were deposited *via* aerosol deposition, as in Figure 2B. Figure 2C shows a coherent interface between the integrated cell and the underlying (featureless) lipid−silica thin film mesophase and a smooth

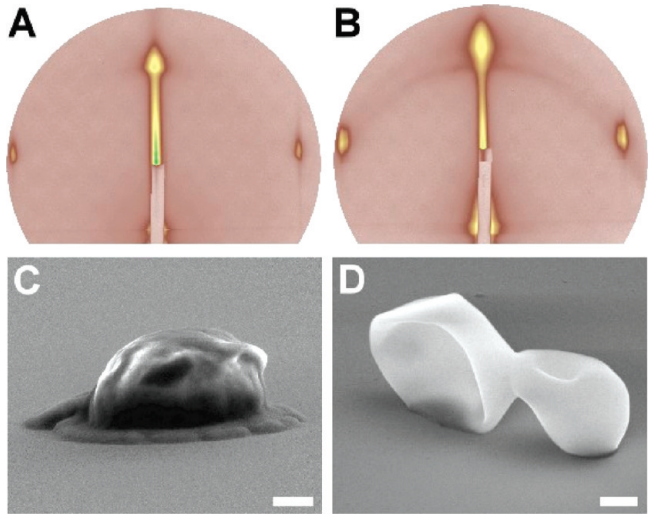

Figure 2. Grazing-incidence small-angle X-ray scattering (GISAXS) patterns of lipid-templated mesoporous silica films: (A) pristine film, (B) film following self-encapsulation of *S. cerevisiae* cells. (C) SEM image of a single yeast cell encapsulated into the lipid-templated silica matrix. (D) SEM image of two yeast cells introduced to a clean silicon substrate without a lipid-templated mesoporous silica thin film. Scale bars = 1 μm.

conformal coating overtop the cell. At the base of the encapsulated cell, a raised region is observed corresponding to deposition of silica and lipid concentrate driven toward the cells during droplet evaporation, as described previously (Scheme 1c). Interestingly, the shape of integrated cells investigated using SEM appeared relatively spherical, indicating that the native morphology of the yeast cells, in large part, was retained during the encapsulation process. Additionally, the encapsulated cell morphology was maintained under continuous exposure to vacuum and electron beam irradiation over the course of SEM imaging (without any additional sample preparation). This is in contrast to SEM images of *S. cerevisiae* cells introduced onto bare silicon substrates without lipid−silica thin films. As shown in Figure 2D, cells appear non-adherent and exhibit signs of severe desiccation with significantly collapsed morphologies. Preservation of cell morphology through silica encapsulation bears some analogy to certain marine organisms (*e.g.*, diatoms, radiolarians, and sponges) that fix silica on their cell surfaces, forming an artificial exoskeleton, which can preserve cell morphology and function under harsh conditions.

3D Bio/Nano Interface. Hyperspectral confocal fluorescence microscopy was used to further characterize the three-dimensional structure of the lipid/silica-encapsulated *S. cerevisiae* cells. For films prepared with the pH-sensitive fluorescent probe, Oregon Green (OG), multivariate curve resolution (MCR) identified two independently varying spectral components corresponding to the *S. cerevisiae* cellular autofluorescence and to OG fluorescence. Spectral components are presented in the Supporting Information, Figure S1. Although the autofluorescence and OG components are highly overlapped, the hyperspectral imaging technique can clearly separate the fluorophores and produce cross-talk free images of the location and intensity of the fluorophores within the images. Figure 3A shows RGB images at various confocal cross sections (red corresponding to the autofluorescence, green corresponding to OG) of a cluster of three encapsulated *S. cerevisiae* cells. The intensity of OG fluorescent emission decreases as the pH is lowered from approximately pH 6 to 3 with total quenching of fluorescence at highly acidic pH (≤2). Consistent with our previous results,[27,28] encapsulated cells form a three-dimensional gradient in pH from approximately pH 3 in the acidic silanol-terminated thin film silica matrix to pH 5.5 at the encapsulated cell surface. This gradient appears to be confined to the <1 μm region of reconstructed lipid/silica surrounding the encapsulated cells. The concentration of *di*C_6 PC lipid in the bulk film and near encapsulated cells was also investigated using hyperspectral imaging. Figure 3B is a false-colored image depicting the concentration of *di*C_6 PC lipid near the base of a single yeast cell. The concentration of lipid surrounding the cell was determined by calibrating TAMRA fluorescence intensi-

ties obtained from the images of solutions with known TAMRA-*di*C_6 PC concentrations at the same microscope settings. Figure 3B shows that the total lipid concentration in the bulk film was 200−250 mg/mL. This is an approximate 10-fold increase in lipid concentration compared to the initial concentration in the sol precursor solution used to produce the film. This observation is consistent with the expected increase in concentration of sol precursor solution components during EISA. Also apparent is a gradient in lipid concentration showing localization of the lipid near the encapsulated cell. Similar to the observations with OG, this gradient in lipid concentration extends below and above the cells and also extends much further into the bulk film. We have previously shown that lipid accumulation at the cellular surface serves to interface encapsulated *S. cerevisiae* with the inorganic silica host matrix.[27,28] Further, as film nanostructure is driven by concentration-dependent lipid self-assembly, we expect this lipid gradient region to correspond to the interface between the hexagonally structured bulk film and the lamellar structure encapsulating the cells. We are currently investigating the structure of this interface region.

The cell-directed integration process can also reorganize, three-dimensionally, nanoscale components introduced into the original lipid−silica thin film mesophase. Figure 3C,D shows hyperspectral confocal images of a cluster of *S. cerevisiae* cells encapsulated within a film prepared with amino-derivatized polyethylene glycol coated quantum dots (655 nm emission). Figure 3C is a false-colored image depicting the fluorescence intensity of the quantum dots present in the lipid−silica matrix. Much like lipids (Figure 3B), the higher fluorescence intensity in the region local to the cells, as compared to the bulk film, shows Qdots to be localized near and around the cells during integration. It also appears that some portion of the Qdots were endocytosed by some of the *S. cerevisiae* cells, showing that the surface of the encapsulated cells remains accessible to and interacts with the nanoparticles concentrated at their surfaces during integration.

Two distinct 655 nm Qdot spectral components were identified from the sample imaged in Figure 3C. Pure component spectra are shown in Figure S2 (Supporting Information). The red spectrum corresponds to the spectral component associated with the 655 nm Qdot spectrum. The green spectrum was obtained by removing the non-negativity constraint from the MCR analysis. This derivative-looking component, when linearly combined with the quantum dot spectral component, models a shift in the quantum dot spectrum. An extensive description of this modeling approach can be reviewed in Haaland *et al*.[42] Figure 3D is a RGB image in which the two spectral components are false-colored showing 655 nm Qdots (green) and 655 nm Qdots that have a red-shifted spectrum (red). Interestingly, using this quantum dot spectra shift information, two different environments can be distinguished within Figure 3D. The spectrum of 655 nm Qdots localized near the yeast cells was red-shifted 7 nm, while the typical 655 nm Qdot spectrum was observed in the bulk film. To determine the source of this spectral shift, 655 nm Qdot spectra were obtained for Qdots in solutions at pH values 3−8 and in solution with *di*C_6 PC lipid. As shown in Figure S3A, no significant shift in 655 nm Qdot spectrum was observed over the studied pH range, indicating that the local gradient in pH near encapsulated cells does not contribute significantly to this shift. However, in the presence of *di*C_6 PC lipid, a red shift in the 655 nm Qdot spectrum of 2 nm was observed (Figure S3B, ~7 mg/mL lipid). From these data, we conclude that the shift in 655 nm Qdot spectra in the lipid−silica

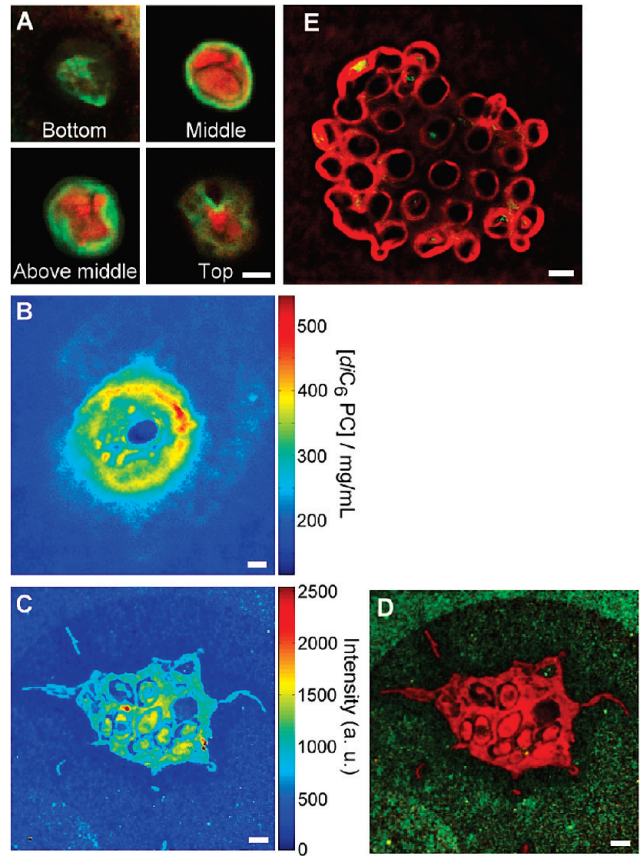

Figure 3. (A−D) False-colored hyperspectral confocal fluorescence images of yeast cells encapsulated in lipid−silica matrices. (A) Confocal slices from a cluster of three *S. cerevisiae* cells (red) encapsulated in a *di*C_6 PC-templated silica film containing the pH-sensitive probe, Oregon Green (green). (B) Confocal slice near the base of a single yeast cell entrapped in a *di*C_6 PC-templated silica film (TAMRA-*di*C_6 PC accounts for 0.1% of total lipid) showing localization of lipid near the cell. Color corresponds to lipid concentration, increasing from blue to red. (C) Confocal slice near the base of a cluster of *S. cerevisiae* cells encapsulated in a lipid−silica matrix containing 655 nm Qdots. Color corresponds to Qdot fluorescence intensity, increasing from blue to red. (D) Two distinct spectra from Qdots in the sample from panel (C) were identified: typical 655 nm Qdot spectrum (green), and Qdot spectrum red-shifted by 7 nm (red). (E) Confocal fluorescence image showing conformal liposome fusion with yeast cells upon integration into the lipid-templated silica film. POPC liposomes (6% Texas Red-labeled DHPE) were introduced to the film with the yeast cell suspension. Scale bars = 3 μm.

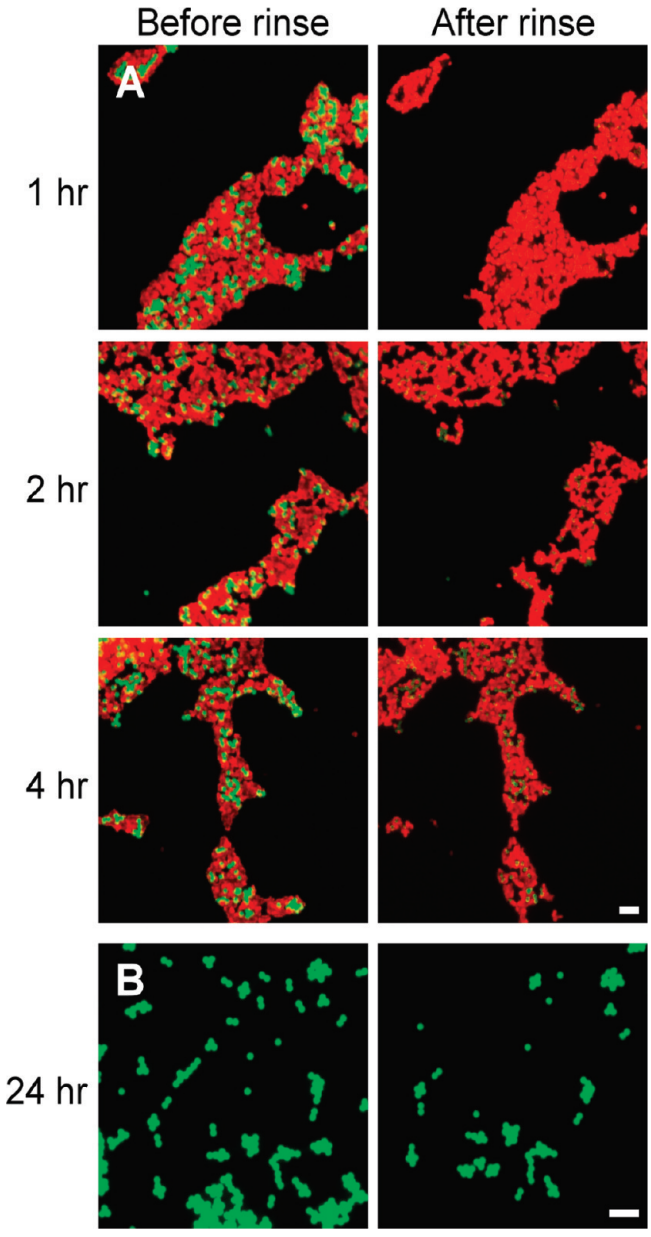

Figure 4. Fluorescence microscopy images of (A) a mixture of *S. cerevisiae* (Cyto64 stained, red emission) and cell surrogates (latex beads, green emission) and (B) latex beads in the absence of cells that were allowed to integrate into lipid templated silica films for 1, 2, 4, or 24 h, after which the films were rinsed to remove non-integrated material. The majority of *S. cerevisiae* cells are not removed by rinsing, while beads are easily washed away under time scales shorter than that required for silica condensation. Scale bars = 25 μm.

cell matrix is largely due to Qdot interactions with the lipid localized near the cells during self-encapsulation. Also, the lack of spectral shift for Qdots in the bulk film indicates that Qdots in this region have little contact with *di*C_6 PC lipid. This is consistent with observations that lipid is quickly solubilized from the film upon introduction of an aqueous droplet. It may also indicate that amino-derivatized PEG-coated Qdots reconstituted near the cell surface during integration are incorporated in a more hydrophilic environment than in the original film.

Nanocomponents introduced with the aqueous cell suspension to lipid-templated films show preferential localization at the cell surface upon integration. Figure 3E shows that addition of palmitoyloleoyl phosphatidylcholine (POPC) liposomes to the yeast cell suspension, followed by deposition onto the silica film, resulted in fusion of liposome lipid (6% Texas Red-labeled DHPC, red emission) with the yeast cell surface. The thickness of liposome layer suggests that multiple fusion steps have occurred during integration, forming yeast-supported multilayers. We have previously reported that liposome fusion with yeast cells in buffered solutions does not occur in the presence of *di*C_6 PC lipid nor under the pH range observed in this system.[43] These results demonstrate the importance of the cell-directed integration process, where long- and short-chain lipids are concentrated within a pH gradient, in forming yeast-supported lipid multilayers from liposomes. This system could provide a simple means to introduce other functional components to the cell surface, including exogenous membrane-bound proteins as we have previously reported utilizing our original cell-directed assembly approach.[43] In contrast to cell-directed assembly of bulk systems, when introduced with yeast cells onto a lipid-templated silica film, liposome lipid localization shows improved conformity with the cell surface. This improved conformity may result from *di*C_6 PC acting as a detergent that, upon droplet evaporation and cell-directed integration, reaches saturated concentration near the cells. This causes destabilization of the colocalized liposomes,[44] facilitating fusion of liposomes with other liposomes and formation of yeast-supported multilayers with prioritized localization of longer-chain lipids at the cell surface within the lipid-rich silica shell.

Living-Cell-Directed Integration. The capability of viable cells to actively facilitate their integration was demonstrated by depositing an aqueous mixture of yeast cells and neutrally charged latex beads, serving as yeast cell surrogates (equivalent vol fraction), onto a weakly condensed lipid-templated silica film (30 min aging from film formation). Following evaporation of the yeast−bead mixture, the samples were aged for an additional 1, 2, or 4 h and then rinsed thoroughly to remove non-integrated material. Images taken before and after rinsing (Figure 4A) show that 1 h following droplet deposition nearly all yeast cells (red emission) were retained in the film, while 95 ± 3% of latex beads (green emission) were removed by rinsing. Samples allowed to age for 2 and 4 h also showed nearly complete integration of cells, but greater amounts of beads were retained at 46 ± 7 and 73 ± 13%, respectively. For aging times on the order of those required for complete condensation of the reconstituted lipid/silica concentrate (24−48 h), 52 ± 12% of the beads remained post-rinsing (Figure 4B). As both *S. cerevisiae* cells and latex beads were surrounded by soluble silica and lipid concentrate during the initial stage of evaporation of the

cell/bead dispersion, these data indicate that cells uniquely promote their integration. We attribute this cell-directed integration to the ability of cells to actively develop a pH gradient that catalyzes silica condensation within a thin three-dimensional volume surrounding the cells. Unlike *S. cerevisiae*, no pH gradient was observed near latex beads introduced to lipid−silica films. As the rate of silica condensation is a strong function of pH and increases significantly between pH 3 and 6,[45] it is likely that the development of the localized pH gradient governs microorganism self-encapsulation within silica.

Self-Catalyzed Silica Condensation. To further elucidate the importance of the active development of a localized pH gradient to cellular integration, we investigated integration under conditions of inhibited cellular response to osmotic stress (osmotic clamp). We have previously reported that viable cells experience osmotic stress during EISA,[27] rapidly excreting up to 35% of their cytosolic fluid volume in response to changes in turgor pressure in the cell membrane resulting from the increasing concentration of soluble silica and salts in the evaporating sol.[46] This results in an increase of water volume in the surrounding ~2 μm thick region of the matrix by more than 60%, creating a gradient in pH in the immediate vicinity of a cell. Therefore, suppressing cellular response to osmotic stress should prevent the formation of this pH gradient and consequently inhibit the proposed self-catalyzed cellular integration process.

Osmotic clamp was induced by adding 2% (vol) of the osmolyte, DMSO, to a split sample of yeast cells in aqueous suspension. This low concentration of DMSO has been shown to significantly inhibit osmotic equilibration due to its high osmolarity and rapid transport rate, while not significantly affecting the metabolic state of the cells.[47,48] Both the control cells (without DMSO) and cells under osmotic clamp were deposited onto weakly condensed lipid-templated silica films and allowed to age for 1 or 2 h, after which the substrates were rinsed thoroughly to remove non-integrated material. The percentage of retained cells under both conditions is presented in Figure 5A. (Pre- and post-rinsing images for control cells and cells under osmotic clamp are presented in the Supporting Information, Figure S4A,B respectively). Control cells from the split sample showed a high degree of integration into the film for both time points (76 and 96%). In contrast, 87−96% of cells under osmotic clamp were removed from the film, indicating that they failed to integrate. Evidence that cells under this treatment are not completely precluded from responding to osmotic stress is shown by the 9% higher retention of cells between the 1 and 2 h aging periods. Figure 5B shows *S. cerevisiae* cells under osmotic clamp introduced to lipid/silica films containing the pH-sensitive probe OG. Prior to rinsing (which removes these clamped cells), we do not observe a gradient in pH (compare with Figure 3A). Rather, we find a uniform pH throughout the sample that corresponds to the pH of the bulk lipid−silica matrix (pH ~3, Figure 5B). Evidence that the integration process is actively directed by living cells is presented in Figure 5C, where we substituted apoptotic *S. cerevisiae* (*i.e.*, those undergoing programmed cell death stimulated by rapid heating to 95 °C), for stationary phase yeast used in the previous experiments. Apoptotic yeast were introduced to a weakly condensed lipid−silica film as before, followed by 2 h of aging and rinsing. As shown in Figure 5A, less than 3% of apoptotic yeast introduced to the film integrated. Figure 5C compares pH gradient development in active and apoptotic yeast introduced to OG-

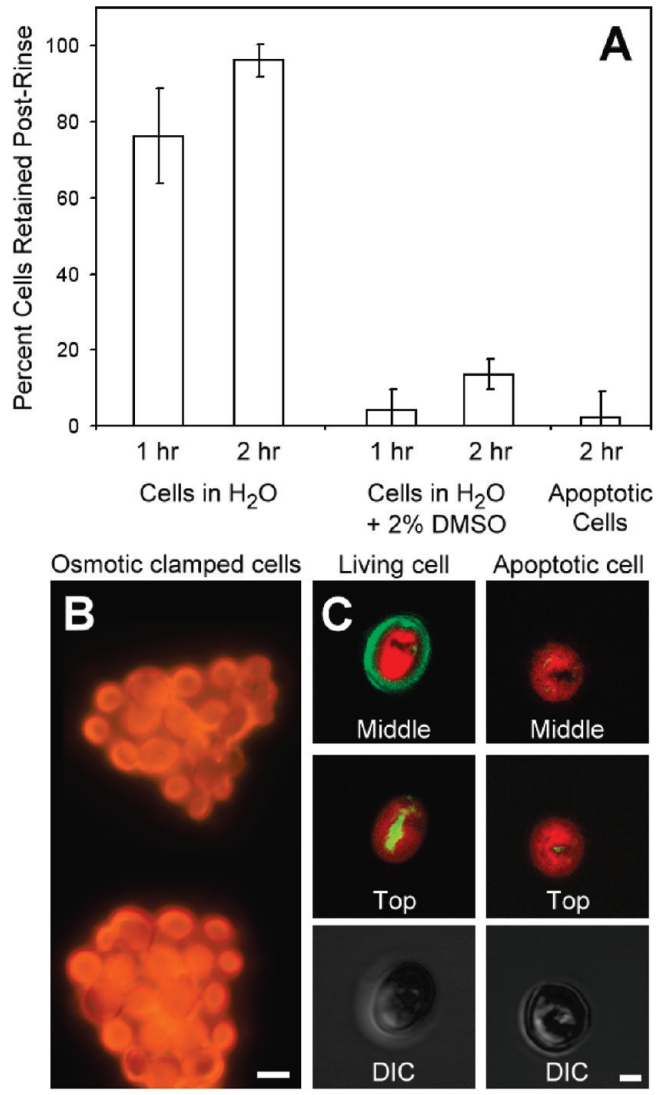

Figure 5. (A) Percent of *S. cerevisiae* cells that integrated into lipid-templated silica films from samples containing cells in water only (control), cells in water with 2% DMSO (cells under osmotic clamp), and apoptotic cells in water (heat shock). Cells were allowed to integrate for 1 or 2 h, after which samples were rinsed to remove non-integrated material. Error bars are the standard deviation of measurements obtained from three or more samples. (B,C) *S. cerevisiae* cells introduced to a lipid-templated mesoporous silica film containing OG prior to rinsing. (B) Fluorescence microscopy image of *S. cerevisiae* cells under osmotic clamp (Cyto64 stained, two separate fields). Scale bar = 3 μm. (C) Confocal fluorescence and DIC images of a single living or apoptotic (heat shock) *S. cerevisiae* cell (Cyto64 stained). Scale bar = 1 μm.

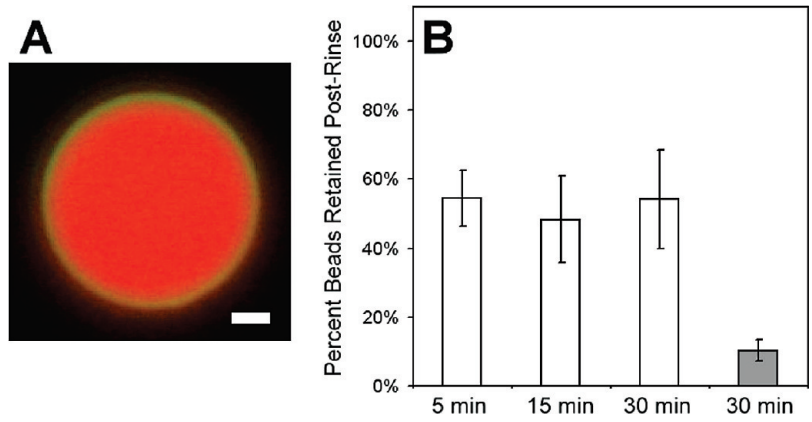

Figure 6. (A) Lysozyme protein-conjugated fluorescent orange 5 μm beads. Lysozyme conjugation verified by subsequent treatment with NHS ester AlexaFluor 488 (green emission). Scale bar = 1 μm. (B) Percent of lysozyme−bead conjugates that integrated into weakly condensed (white bars) and fully condensed (gray bar) lipid-templated silica films. Lysozyme−bead conjugates were allowed to integrate for 5, 15, or 30 min, after which samples were rinsed to remove non-integrated material. Error bars are the standard deviation of measurements obtained from three or more samples.

containing lipid−silica films prior to rinsing. We observe no pH gradient, in contrast to the active yeast (Figures 5C and 3A), and the surface of the apoptotic yeast appears collapsed because it does not catalyze 3D integration within a protective silica shell.

The ability of synthetic and natural polymers possessing amine functional groups to catalyze silica condensation has been widely studied[49,50] and was investigated as a parallel mechanism for cell-directed silica condensation and self-integration. Strong attractive electrostatic interactions and weak hydrogen bonding between polycationic macromolecules and polysilicic acid has been shown to induce silica polymerization and precipitation.[51] As the cell wall of *S. cerevisiae* is known to display a multitude of proteins,[52] polycationic and/or amine functional regions exist on the exterior of the cell. The possible contribution of cationic protein residues to cell-directed catalysis of silica and self-encapsulation, along with electrostatic interactions between these residues and the negatively charged lipid−silica film, were examined using lysozyme protein-coated beads. In the presence of soluble silica, lysozyme is known to induce local silicate condensation forming precipitated silica particles.[53]

Carboxylic acid functionalized fluorescent orange beads (5 μm diameter) were conjugated to lysozyme proteins *via* carbodiimide chemistry (see Experimental Section). Lysozyme conjugation was verified by subsequent treatment with NHS ester AlexaFluor 488 (green emission), which bound to free amines present on the surface of lysozyme, as shown in Figure 6A. Aqueous suspensions of lysozyme−bead conjugates were deposited onto weakly condensed lipid-templated silica films (aged 30 min prior to bead deposition) and aged for 5, 15, or 30 min post-droplet evaporation, followed by thorough rinsing. Interestingly, nearly 50% of the lysozyme−bead conjugates under each incubation period remained in the film, as shown in Figure 6B. These results differ significantly from those obtained with latex beads which showed only ~5% integration efficiency (Figure 4A). This demonstrates that lysozyme protein significantly interacts with the lipid−silica film. The extent of this interaction that can be attributed to electrostatic binding between the positively charged lysozyme molecules (pI ~ 10) and the lipid−silica film, independent of polycationic residue-induced catalysis of silica condensation, was investigated by introducing lysozyme−bead conjugates to a lipid-templated mesoporous silica film that was previously allowed to fully condense. As only trace levels of silica precursors are solubilized from the fully condensed film, silica condensation cannot contribute to the population of lysozyme−bead conjugates that remain post-rinsing. As shown in Figure 6B (gray bar) approximately 10% of the lysozyme−bead conjugates remain. Retention of this lower population of lysozyme−bead conjugates is attributed to the strong electrostatic interactions between lysozyme and the silica film. Further, this result shows that the larger fraction of lysozyme−bead conjugates retained upon introduction to a weakly condensed lipid−silica film can be attributed to polycationic residue-catalyzed silica condensation.

These data provide evidence that polycationic and/or amine functional regions on the exterior of *S. cerevisiae* may contribute to self-integration. It should also be noted that in the case of living microorganism encapsulation, a neutral pH develops near the cellular surface which would increase the rate of cell wall protein/peptide-induced silica condensation.[51] However, these data, combined with the poor integration of *S. cerevisiae* under osmotic clamp or apoptotic conditions, both of which still display proteins, albeit at low pH, indicate that this is a minor mechanism under the time scales investigated in this study. Finally, the localized lipid lamellar interface formed during cellular integration may serve to physically isolate the cell surface and surface proteins from silica precursors, further re-

ducing the impact of polycationic macromolecule-induced silica condensation on cellular integration.

Integrated Cell Viability. Viability of integrated cells depended strongly on storage conditions. Substrates with integrated cells placed into buffer or media (YPD) approximately 35 min post-droplet evaporation showed 15 ± 6.9% viability as measured by CFDA/PI assay (see Experimental Section). If maintained under these solutions at room temperature, the thin lipid−silica shell encapsulating the cells slowly dissolved freeing yeast cells between 3 and 5 days post-integration. If under YDP medium, released cells would replicate, demonstrating that the cells do remain viable and culturable following cell-directed integration into the lipid−silica mesophase film.

Substrates with integrated cells stored under dry room temperature conditions showed significant loss in viability over the first few hours post-integration with less than 4% viable cells after 24 h. However, addition of trehalose to the matrix, a disaccharide known to provide improved tolerance to desiccation, significantly improved viability of integrated cells when stored dry. If trehalose was added directly to the aqueous suspension of cells, followed by deposition onto the lipid−silica film, we found that the droplet did not completely evaporate, forming a gel phase that prevented cellular integration into the film. Alternatively, addition of trehalose to the lipid−silica precursor solution, followed by film formation, allowed for integration of cells into the trehalose containing film. We propose that trehalose was solubilized from the film by the aqueous cell suspension and accumulated near the cells in a manner similar to that observed for solubilized lipid and silica. The lower concentration of trehalose solublized from the film did not form a gel phase, allowing development of evaporation-induced osmotic stress and pH gradients required for integration. A strong dependence of viability on trehalose film concentration was observed and is shown in Figure S5 (Supporting Information). At 45 mg/mL trehalose in the lipid−silica precursor solution, 23 ± 10% of cells remained viable after dry storage at room temperature for 7 days. In these experiments 2×10^5 cells/cm^2 are initially integrated into the lipid−silica mesophase films, leaving approximately 4.5×10^4 viable cells/cm^2 following 7 days of dry storage. This considerable population of viable cells is sufficient for subsequent use or experimentation.

CONCLUSIONS

In summary, we have described a unique method in which cells introduced onto a solid-state lipid−silica mesophase film actively reconstruct the surface to create a fully 3D bio/nano interface composed of a lipid-rich silica shell that coherently interfaces the cells with the nanostructured inorganic matrix. We attribute this cell-directed integration to the ability of cells to actively develop a pH gradient in response to evaporation-induced osmotic stress, which catalyzes silica condensation within a thin three-dimensional volume surrounding the cells. Auxiliary nanocomponents added to the lipid/silica mesophase film, or introduced with the cells, were localized at the cellular surface, providing a means to introduce foreign functionalities, which remained accessible to and interacted with the cellular surface. This process is simple and does not expose cells to toxic solvents, chemical byproducts, or drying stresses, preserving the original cell morphology. We expect this method to be general and adaptable to other bacterial and fungal cells and even mammalian cells. It promises to be useful as a new technique for integrating bio with nano, impacting fundamental studies in nanoparticle toxicology, cell−cell signaling, and development of bioelectronics and cell-based biosensors.

EXPERIMENTAL SECTION

Materials. Aqueous solutions were prepared with 18 MΩ water using a Barnstead Nanopure water purifier (Boston, MA). Tetraethylorthosilicate (TEOS), tetramethylorthosilicate (TMOS), sodium molybdate, ascorbic acid, lysozyme (from chicken egg white), and hydrochloric acid (HCl) were purchased from Sigma-Aldrich (St. Louis, MO). 2-[4-(2-Hydroxyethyl)-1-piperazine]ethanesulfonic acid (HEPES), 1-ethyl-3-[3-dimethylaminopropyl]carbodiimide hydrochloride (EDC), 4-aminobenzoic acid, *N*-hydroxysuccinimide (NHS), and ethanol (absolute) were obtained from Acros Organics (Beel, Belgium). Phosphate buffer saline (PBS) solution, pH 7.4 (11.9 mM phosphates, 137 mM NaCl, and 2.7 mM KCl), sodium hydroxide (NaOH), potassium hydroxide (KOH), and dimethyl sulfoxide (DMSO) were purchased from Fischer Scientific (Pittsburgh, PA). 1,2-Dihexanoyl-*sn*-glycero-3-phosphocholine (*di*C_6 PC), 1-hexanoyl-2-{6-[(7-nitro-2-1,3-benzoxadiazol-4-yl)amino]hexanoyl}-*sn*-glycero-3-phosphocholine (NBD-*di*C_6 PC), 1-hexanoyl-2-{6-[(5-(and-6)-carboxytetramethylrhodamine)amino]hexanoyl-*sn*-glycero-3-phosphocholine (TAMRA- *di*C_6 PC), and palmitoyloleoyl phosphatidylcholine (POPC) were obtained from Avanti Polar Lipids (Alabaster, AL). 2′,7′-Difluorofluorescein Oregon Green 488 (OG), AlexaFluor 488 carboxylic acid succinimidyl ester (NHS-AlexaFluor 488), amino-derivatized polyethylene glycol (PEG)-coated 655 nm quantum dots (655 nm Qdots), Texas Red-labeled DHPE, and Funga Light CFDA/PI yeast viability kit were from Invitrogen (Carlsbad, CA). Latex beads (5 μm, fluorescent green) were from Duke Laboratories (now part of Thermo Scientific). Carboxyl -functionalized Suncoast Yellow beads (5 μm, fluorescent orange) were from Bangs Laboratories (Fishers, IN).

Lipid-Templated Silica Film Formation. Prehydrolyzed TEOS stock solutions (A2**) were prepared by refluxing 61 mL of TEOS, 61 mL of ethanol (absolute), 4.9 mL of nanopure water, and 0.2 mL of 0.07 N HCl (molar ratio 1:4:1:5 × 10^{-5}) for 90 min at 60 °C. Stock solutions were stored at −20 °C. A2** stock was used to prepare the precursor sol solution by adding 0.25 mL of A2**, 0.20 mL of ethanol (absolute), 0.16 mL of 0.05 N HCl, and 0.40 mL of nanopure water (molar ratio of 1 TEOS/4.0 ethanol/2.0 water/0.005 HCl) to 30 mg of *di*C_6 PC. This solution was allowed to age at room temperature for 20 min. Following aging the solution was spin-coated onto 25 mm No. 1.5 round glass coverslips which had been pretreated in 0.1 M KOH for at least 2 h, washed with 1% Alconox in nanopure water, and rinsed with nanopure

water and ethanol, and then cleaned in a UVO cleaner (Jelight model 342) for 5 min. Spin coating occurred at 1500 rpm for 30 s (Laurell model WS-400B) at <20% relative humidity. Films containing fluorescently labeled lipid (0.1% of total lipid) were prepared as described above with the addition of 0.03 mg of either NBD- or TAMRA-*di*C_6 PC to the sol precursor solution prior to the 20 min room temperature incubation. Films containing OG or 655 nm Qdots were prepared as described above with the addition of 20 μL of OG solution (13.5 mM) or 10 μL of 655 nm Qdot solution (8 μM) to 1 mL of the sol precursor solution prior to the 20 min room temperature incubation.

Cell Self-Integration. *S. cerevisiae* (strain S288C, Invitrogen) was grown in glucose-based rich medium (YPD) to G0 or stationary phase. Cells were collected by centrifugation, washed three times in nanopure water, and resuspended in nanopure water. Aqueous suspensions of yeast were introduced onto preformed lipid-templated mesoporous silica films 30−120 min after formation in 0.5 μL droplets (10^5−10^6 cells/mL) and allowed to dry. Once dry, substrates were allowed to rest for given periods of time and then rinsed thoroughly with nanopure water (10 s exposure to water stream, followed by drying with N_2 stream) to remove non-integrated material.

Reduced Molybdic Acid Assay for Soluble Silica Content. The amount of silica removed from the film by a drop of water residing on the film surface was quantified by the reduced molybdic acid assay method.[40,45] This assay is more sensitive then the molybdic acid (MA) test, allowing calibration down to 2 μM of silicic acid. Ten millimolar sodium molybdate was prepared in DI water and pH was adjusted to 1.2 with HCl. Plastic vessels were used to avoid silica contamination. The sample was collected by placing a drop of DI water on the silica−lipid film for 10 min followed by careful removal of 80% of the drop without scratching the film. This sample was incubated overnight after adding 40 μL of 5 mM NaOH to dissolve any silica aggregates. The sample was placed into a 1 mL cuvette, along with 0.8 mL of the sodium molybdate solution, and allowed to incubate for 30 min. Following incubation, 40 μL of 0.5 M ascorbic acid was added to the cuvette. Immediately, the previously clear assay solution started turning blue. Exactly 60 s after ascorbic acid addition, the sample was scanned with the UV−vis spectrophotometer. The scan (500−700 nm) took 12 s. Timing is important as the color intensity of reduced molybdic acid is unstable. Satisfactory linear calibration curves based on hydrolyzed TMOS were obtained with every experiment. Silica concentration in film dissolution samples was determined by least-squares fit to an absorbance curve derived from the calibration data.

Fluorescently Labeled Liposome Formation. Palmitoyloleoyl phosphatidylcholine (POPC) was dissolved in chloroform, dried, and maintained overnight under vacuum to remove residual solvent; 2.5 mg of lipid (including Texas Red-labeled DHPE at 6 wt %) was dissolved in 0.5× PBS, sonicated briefly, and extruded through a 100 nm filter (Millipore) 10 times.

Lysozyme−Bead Conjugation. Carboxyl-functionalized 5 μm diameter beads were diluted 10-fold from stock solution into 1 mL of 10 mM HEPES buffer solution, pH 7.5, containing 10 mM EDC. Following a 20 min incubation, the beads were pelletted by centrifugation and resuspended in 1 mL of 10 mM HEPES buffer, pH 7.5, containing 1.5 mg of lysozyme protein, and incubated for 2−4 h at room temperature. Following conjugation, the beads were washed three times with HEPES solution and stored at 4 °C until use. To verify lysozyme conjugation onto the beads, 10 μL of stock NHS-AlexaFluor 488 solution was added to 1 mL of the lysozyme-conjugated beads in 10 mM HEPES buffer, pH 7.5, for 2−4 h at room temperature. Following incubation, the beads were washed three times with HEPES solution and then imaged.

Atomic Force, Fluorescence, and Scanning Electron Microscopy. Atomic force microcopy was carried out on a MFP-3B Bio AFM (Asylum Research, Santa Barbara, CA) operated in tapping mode in air and in liquid. For imaging in air AC240 TS cantilevers were used (Olympus, k = 2 N/m). For imaging in water, TR400 PB cantilevers (Olympus, k = 0.09 N/m) were used. For applications where film thickness was determined by AFM, an image at least 20 × 20 μm in size was acquired and analyzed. Fluorescence microscopy imaging was performed on an Olympus IX70 microscope and recorded using an Olympus DP71 camera. A JEOL 6701F scanning electron microscope (SEM) operating at 5 kV was used to directly image cells integrated into lipid−silica films without further preparation.

Hyperspectral Confocal Fluorescence Microscopy. A hyperspectral confocal fluorescence microscope was used to image the yeast cells encapsulated in the lipid−silica matrices. This unique microscope, which was designed and built at Sandia,[54] is a fully confocal design capable of collecting 8300 pixels per second. Each pixel consists of 512 emission wavelengths spanning the spectral region of 490−800 nm when the sample is excited using a solid-state 488 nm laser (Coherent, Incorporated). These emission wavelengths are dispersed onto a electron multiplying charge-coupled device (EMCCD) detector using a custom-built high-throughput prism spectrometer. The resolution of this microscope consists of a lateral (x,y) spatial resolution of 0.25 μm, an axial (z) resolution is 0.6 μm and a spectral resolution of better than 3 nm. For the collection of the encapsulated yeast cell samples, a oil immersion 60× objective with a numerical aperture of 1.4 was used to collect the images.

Once the hyperspectral images have been collected, the images are preprocessed to remove unwanted spectral artifacts and then the images are analyzed using multivariate curve resolution (MCR). The preprocessing consisted of the following steps: (1) detection and removal of cosmic spikes collected on the EMCCD, (2) subtraction of the dark image to remove the effects of a structured noise source from the spectral data, and (3) removal of the spectral offset arising from the electronics of the EMCCD. A more detailed description of the preprocessing steps can be found in the experimental section in Jones *et al.*[55] Following these preprocessing steps, MCR analyses of the spectral image data sets were conducted. MCR is a powerful multivariate analysis technique in which the associated algorithms can extract the pure spectral emission and the corresponding intensities of each spectral component for each pixel in the image. In addition, MCR can discover all emitting fluorphores that are above the noise floor without any *a priori* information regarding the sample being imaged (*i.e.*, no information is needed to discover and quantify the fluorophores present in the sample images). Therefore, both known and unknown spectral emissions can be discovered and quantified within the images. Also, unlike most filter-based fluorescence microscopes, it is not necessary to have well-separated fluorophores to obtain quantitative images since the MCR algorithms can significantly reduce the amount of cross-talk between fluorophores. Further information on MCR implementation and decriptions of the MCR software written in Matlab and C code are detailed elsewhere.[42,55−59]

Integrated Yeast Viability Assay. Integrated yeast viability was measured using the Funga Light assay (Invitrogen) containing a cell-permeable nonspecific esterase substrate (acetoxymethyl ester 5-carboxyfluorescein diacetate, CFDA) and a cell membrane integrity indicator (propidium iodide, PI). Viability assay was performed using the manufacturer's protocol with slight modifications. One microliter of CFDA solution (1 mg in 100 μL of DMSO) and 1 μL of PI solution (20 mM in H_2O) were added to 1 mL of 1× PBS, pH 7.4. This solution was carefully pipetted onto substrates containing cells integrated in a lipid−silica film and incubated at room temperature for 45−60 min. Following incubation, cells still under CDFA/PI assay solution were imaged with an inverted fluorescence microscope. Cells with esterase activity and intact membranes fluoresced green and were counted as viable. Cells without esterase activity and damaged membranes fluoresced red and were not counted as viable. Cells with residual esterase activity and damaged membranes fluoresced yellow and were not counted as viable.

Acknowledgment. We thank Michael R. Keenan, Mark Van Benthem, and David K. Melgaard for their contributions in the development of the MCR algorithms and software. We also thank Michael B. Sinclair for use of the hyperspectral confocal microscope. This work was funded by the Defense Treat Reduction Agency (DTRA) Chem. Bio. Basic Research Program Grant B084467I, DoE NNSA Office for Nonproliferation Research and Development (NA-22), the Air Force Office of Science and Research (AFOSR), Sandia's Lab Directed Research and Develop-

ment program, and the DoE Office of Science Basic Energy Sciences Division of Materials Science and Engineering. This work was performed, in part, at the Center for Integrated Nanotechnologies, a U.S. Department of Energy Office of Basic Energy Sciences user facility at Los Alamos National Laboratory (Contract DE-AC52-06NA25396). Sandia National Laboratories is a multiprogram laboratory operated by Sandia Corporation, a wholly owned subsidiary of Lockheed Martin Company, for the U.S. Department of Energy's National Nuclear Security Administration under Contract DE-AC04-94AL85000.

Supporting Information Available: Figures S1−S5, described in the text. This material is available free of charge *via* the Internet at http://pubs.acs.org.

REFERENCES AND NOTES

1. Kandimalla, V. B.; Tripathi, V. S.; Ju, H. Immobilization of Biomolecules in Sol−Gels: Biological and Analytical Applications. *Crit. Rev. Anal. Chem.* **2006**, *36*, 73–106.
2. Salaita, K.; Wang, Y.; Mirkin, C. A. Applications of Dip-Pen Nanolithography. *Nat. Nanotechnol.* **2007**, *2*, 145–155.
3. Dave, B. C.; Dunn, B.; Valentine, J. S.; Zink, J. I. Sol−Gel Encapsulation Methods for Biosensors. *Anal. Chem.* **1994**, *66*, 1120A–1127A.
4. Carballeria, J. D.; Quezada, M. A.; Hoyos, P.; Simeó, Y.; Hernaiz, M. J.; Alcantara, A. R.; Sinisterra, J. V. Microbial Cells as Catalysts for Stereoselective Redox Reactions. *Biotechnol. Adv.* **2009**, *27*, 686–714.
5. Yap, F. L.; Zhang, Y. Proteins and Cell Micropatterning and Its Integration with Micro/Nanoparticles Assembly. *Biosens. Bioelectron.* **2007**, *22*, 775–788.
6. Ispas, C.; Sokolov, I.; Andreescu, S. Enzyme-Functionalized Mesoporous Silica for Bioanalytical Applications. *Anal. Bioanal. Chem.* **2009**, *393*, 543–554.
7. Gupta, R.; Chaudhury, N. K. Entrapment of Biomolecules in Sol−Gel Matrix for Applications in Biosensors: Problems and Future Prospects. *Biosens. Bioelectron.* **2007**, *22*, 2387–2399.
8. Carturan, G.; Toso, R. B.; Boninsegna, S.; Monte, R. D. Encapsulation of Functional Cells by Sol−Gel Silica: Actual Progress and Perspectives for Cell Therapy. *J. Mater. Chem.* **2004**, *14*, 2087–2098.
9. Ellerby, L. M.; Nishida, C. R.; Nishida, F.; Yamanaka, S.; Dunn, B.; Valentine, J. S.; Zink, J. I. Encapsulation of Proteins in Transparent Porous Silicate Glasses Prepared by the Sol−Gel Method. *Science* **1992**, *255*, 1113–1115.
10. Sheldon, R. A. Enzyme Immobilization: The Quest for Optimum Performance. *Adv. Synth. Catal.* **2007**, *349*, 1289–1307.
11. Orive, G.; Hernández, R. M.; Gascón, A. R.; Calafiore, R.; Chang, T. M. S.; de Vos, P.; Hortelano, G.; Hunkeler, D.; Lacík, I.; Pedraz, J. L. History, Challenges and Perspectives of Cell Microencapsulation. *Trends Biotechnol.* **2004**, *22*, 87–92.
12. Orive, G.; Hernández, R. M.; Gascón, A. R.; Calafiore, R.; Chang, T. M. S.; de Vos, P.; Hortelano, G.; Hunkeler, D.; Lacík, I.; Shapiro, A. M. J.; Pedraz, J. L. Cell Encapsulation: Promise and Progress. *Nat. Med.* **2003**, *9*, 104–107.
13. Murua, A.; Portero, A.; Orive, G.; Hernández, R. M.; de Castro, M.; Pedraz, J. L. Cell Microencapsulation Technology: Towards Clinical Application. *J. Controlled Release* **2008**, *132*, 76–83.
14. Carturan, G.; Campostrini, R.; Dirè, S.; Scardi, V.; de Alteriis, E. Inorganic Gels for Immobilization of Biocatalysts: Inclusion of Invertase-Active Whole Cells of Yeast (*Saccharomyces cerevisiae*) into Thin Layers of SiO_2 Gel Deposited on Glass Sheets. *J. Mol. Catal.* **1989**, *57*, L13–L16.
15. Avnir, D.; Coradin, T.; Lev, O.; Livage, J. Recent Bio-applications of Sol−Gel Materials. *J. Mater. Chem.* **2006**, *16*, 1013–1030.
16. Pope, E. J. A.; Braun, K.; Peterson, C. M. Bioartificial Organs I: Silica Gel Encapsulated Pancreatic Islets for the Treatment of Diabetes Mellitus. *J. Sol−Gel Sci. Technol.* **1997**, *8*, 635–639.
17. Chia, S.; Urano, J.; Tamanoi, F.; Dunn, B.; Zink, J. I. Patterned Hexagonal Arrays of Living Cells in Sol−Gel Silica Films. *J. Am. Chem. Soc.* **2000**, *122*, 6488–6489.
18. Nassif, N.; Roux, C.; Coradin, T.; Rager, M.-N.; Bouvet, O. M. M.; Livage, J. A Sol−Gel Matrix to Preserve the Viability of Encapsulated Bacteria. *J. Mater. Chem.* **2003**, *13*, 203–208.
19. Nassif, N.; Bouvet, O.; Rager, M. N.; Roux, C.; Coradin, T.; Livage, J. Living Bacteria in Silica Gels. *Nat. Mater.* **2002**, *1*, 42–44.
20. Conroy, J. F. T.; Power, M. E.; Martin, J.; Earp, B.; Hosticka, B.; Daitch, C. E.; Norris, P. M. Cells in Sol−Gels I: A Cytocompatible Route for the Production of Macroporous Silica Gels. *J. Sol−Gel Sci. Technol.* **2000**, *18*, 269–283.
21. Gill, I.; Ballesteros, A. Encapsulation of Biologicals within Silicate, Siloxane, and Hybrid Sol−Gel Polymers: An Efficient and Generic Approach. *J. Am. Chem. Soc.* **1998**, *120*, 8587–8598.
22. Yu, D.; Volponi, J.; Chhabra, S.; Brinker, C. J.; Mulchandani, A.; Singh, A. K. Aqueous Sol−Gel Encapsulation of Genetically Engineered *Moraxella* spp. Cells for the Detection of Organophosphates. *Biosens. Bioelection.* **2005**, *20*, 1433–1437.
23. Coiffier, A.; Coradin, T.; Roux, C.; Bouvet, O. M. M.; Livage, J. Sol−Gel Encapsulation of Bacteria: A Comparison between Alkoxide and Aqueous Routes. *J. Mater. Chem.* **2001**, *11*, 2039–2044.
24. Finnie, K. S.; Bartlett, J. R.; Woolfrey, J. L. Encapsulation of Sulfate-Reducing Bacteria in a Silica Host. *J. Mater. Chem.* **2000**, *10*, 1099–1101.
25. Campostrini, R.; Carturan, G.; Caniato, R.; Piovan, R.; Filippini, G.; Innocenti, G.; Cappelletti, E. M. Immobilization of Plant Cells in Hybrid Sol−Gel Materials. *J. Sol−Gel Sci. Technol.* **1996**, *7*, 87–97.
26. Muraca, M.; Vilei, M. T.; Zanusso, G. E.; Ferraresso, C.; Boninsegna, S.; Monte, R. D.; Carraro, P.; Carturan, G. SiO_2 Entrapment of Animal Cells: Liver-Specific Metabolic Activities in Silica-Overlaid Hepatocytes. *Artif. Organs* **2002**, *26*, 664–669.
27. Baca, H. K.; Ashley, C.; Carnes, E.; Lopez, D.; Flemming, J.; Dunphy, D.; Singh, S.; Chen, Z.; Liu, N. G.; Fan, H. Y.; Lopez, G. P.; Brozik, S. M.; Werner-Washburne, M.; Brinker, C. J. Cell-Directed Assembly of Lipid−Silica Nanostructures Providing Extended Cell Viability. *Science* **2006**, *313*, 337–341.
28. Baca, H. K.; Carnes, E.; Singh, S.; Ashley, C.; Lopez, D.; Brinker, C. J. Cell-Directed Assembly of Bio/Nano Interfaces—A New Scheme for Cell Immobilization. *Acc. Chem. Res.* **2007**, *40*, 836–845.
29. Brinker, C. J.; Lu, Y. F.; Sellinger, A.; Fan, H. Y. Evaporation-Induced Self-Assembly: Nanostructures Made Easy. *Adv. Mater.* **1999**, *11*, 579–585.
30. Carnes, E. C.; Lopez, D. M.; Donegan, N. P.; Cheung, A.; Gresham, H.; Timmins, G. S.; Brinker, C. J. Confinement-Induced Quorum Sensing of Individual *Staphylococcus aureus* Bacteria. *Nat. Chem. Biol.* **2010**, *6*, 41–45.
31. Stevens, M. M.; George, J. H. Exploring and Engineering the Cell Surface Interface. *Science* **2005**, *310*, 1135–1138.
32. Zhange, S. G. Beyond the Petri Dish. *Nat. Biotechnol.* **2004**, *22*, 151–152.
33. Stoodley, P.; Sauer, K.; Davies, D. G.; Costerton, J. W. In *Annual Review of Microbiology*; Ornston, L. N., Balows, A., Gottesman, S., Eds.; Annual Reviews: Palo Alto, CA, 2002; Vol. 56, pp 187−209.
34. Raghavan, S.; Chen, C. S. Micropatterned Environments in Cell Biology. *Adv. Mater.* **2004**, *16*, 1303–1313.
35. Hu, H.; Larson, R. G. Analysis of the Effects of Marangoni Stresses on the Microflow in an Evaporating Sessile Droplet. *Langmuir* **2005**, *21*, 3972–3980.
36. Kuncicky, D. M.; Velev, O. D. Surface-Guided Templating of Particle Assemblies inside Drying Sessile Droplets. *Langmuir* **2008**, *24*, 1371–1380.
37. Truskett, V. N. Influence of Surfactants on an Evaporating Drop: Fluorescence Images and Particle Deposition Patterns. *Langmuir* **2003**, *19*, 8271–8279.

38. Deegan, R. D.; Bakajin, O.; Dupont, T. F.; Huber, G.; Nagel, S. N.; Witten, T. A. Capillary Flow as the Cause of Ring Stains from Dried Liquid Drops. *Nature* **1997**, *389*, 827–829.
39. Brinker, C. J.; Scherer, G. *Sol−Gel Science: The Physics and Chemistry of Sol−Gel Processing*; Academic: Boston, MA, 1990.
40. Andersson, L. H. Determination of Silica. VII. Some Experiments with the Gravimetric Silica Determinations. *Arkiv för Kemi* **1962**, *19*, 223–233.
41. Doshi, D. A.; Gibaud, A.; Goletto, V.; Lu, M.; Gerung, H.; Ocko, B.; Han, S. M.; Brinker, C. J. Peering into the Self-Assembly of Surfactant Templated Thin-Film Mesophases. *J. Am. Chem. Soc.* **2003**, *125*, 11646–11655.
42. Haaland, D. M.; Jones, H. D. T.; Van Benthem, M. H.; Sinclair, M. B.; Melgaard, D. K.; Stork, C. L.; Pedroso, M. C.; Liu, P.; Brasier, A. R.; Andrews, N. L.; Lidke, D. S. Hyperspectral Confocal Fluorescence Imaging: Exploring Alternative Multivariate Curve Resolution Approaches. *Appl. Spectrosc.* **2009**, *63*, 271–279.
43. Carnes, E. C.; Harper, J. C.; Ashley, C. E.; Lopez, D. M.; Brinker, L. M.; Liu, J.; Singh, S.; Brozik, S. M.; Brinker, C. J. Cell-Directed Localization and Orientation of a Functional Foreign Transmembrane Protein within a Silica Nanostructure. *J. Am. Chem. Soc.* **2009**, *131*, 14255–14257.
44. Rigaud, J.-L.; Paternostre, M.-T.; Bluzat, A. Mechanisms of Membrane Protein Insertion into Liposomes during Reconstitution Procedures Involving the Use of Detergents. 2. Incorporation of the Light-Driven Proton Pump Bacteriorhodopsin. *Biochemistry* **1988**, *27*, 2677–2688.
45. Iler, R. L. *The Chemistry of Silica*; John Wiley & Sons: New York, 1979.
46. de Maranon, I. M.; Marechal, P.-A.; Gervais, P. Passive Response of *Saccharomyces cerevisiae* to Osmotic Shifts: Cell Volume Variations Depending on the Physiological State. *Biochem. Biophys. Res. Commun.* **1996**, *227*, 519–523.
47. Yang, B.; Kim, J. K.; Verkman, A. S. Comparative Efficacy of $HgCl_2$ with Candidate Aquaporin-1 Inhibitors DMSO, Gold, TEA^+ and Acetazolamide. *FEBS Lett.* **2006**, *580*, 6679–6684.
48. de Bruijne, A. W.; van Steveninck, J. Lysis of Yeast Cells and Erythrocytes by Dimethylsulfoxide. *Biochem. Pharmacol.* **1972**, *21*, 153–162.
49. Patwardhan, S. V.; Clarson, S. J.; Perry, C. C. On the Role(s) of Additives in Bioinspired Silicification. *Chem. Commun.* **2005**, 1113–1121.
50. Lopez, P. J.; Gautier, C.; Livage, J.; Coradin, T. Mimicking Biogenic Silica Nanostructures Formation. *Curr. Nanosci.* **2005**, *1*, 73–83.
51. Coradin, T.; Livage, J. Aqueous Silicates in Biological Sol−Gel Applications: New Perspectives for Old Precursors. *Acc. Chem. Res.* **2007**, *40*, 819–826.
52. Ruiz-Herrera, J. *Fungal Cell Wall: Structure, Synthesis, and Assembly*; CRC: Boca Raton, FL, 1992.
53. Coradin, T.; Coupé, A.; Livage, J. Interactions of Bovine Serum Albumin and Lysozyme with Sodium Silicate Solutions. *Colloids Surf., B* **2003**, *29*, 189–196.
54. Sinclair, M. B.; Haaland, D. M.; Timlin, J. A.; Jones, H. D. T. Hyperspectral Confocal Microscope. *Appl. Opt.* **2006**, *45*, 6283–6291.
55. Jones, H. D. T.; Haaland, D. M.; Sinclair, M. B.; Melgaard, D. K.; Van Benthem, M. H.; Pedroso, M. C. Weighting Hyperspectral Image Data for Improved Multivariate Curve Resolution Results. *J. Chemom.* **2008**, *22*, 482–490.
56. Van Benthem, M. H.; Keenan, M. R.; Haaland, D. M. Application of Equality Constraints on Variables During Alternating Least Squares Procedures. *J. Chemom.* **2002**, *16*, 613–622.
57. Van Benthem, M. H.; Keenan, M. R. Fast Algorithm for the Solution of Large-Scale Non-negativity-Constrained Least Squares Problems. *J. Chemom.* **2004**, *18*, 441–450.
58. Kotula, P. G.; Keenan, M. R.; Michael, J. R. Automated Analysis of SEM X-ray Spectral Images: A Powerful New Microanalysis Tool. *Microsc. Microanal.* **2003**, *9*, 1–17.
59. Ohlhausen, J. A. T.; Keenan, M. R.; Kotula, P. G.; Peebles, D. E. Multivariate Statistical Analysis of Time-of-Flight Secondary Ion Mass Spectrometry Images Using AXSIA. *Appl. Surf. Sci.* **2004**, *231/232*, 230–234.